

A Novel and Highly Efficient Indolyl-Based Electrolyte for Mg Batteries

Steve Zaubitzer, Saustin Dongmo, Philipp Schüler, Sven Krieck, Florian Fiesinger, Daniel Gaissmaier, Matthias van den Borg, Timo Jacob, Matthias Westerhausen, Margret Wohlfahrt-Mehrens, and Mario Marinaro*

Magnesium-based batteries are one of the most promising candidates as postlithium electrochemical energy storage devices. Despite considerable research progress, suitable electrolytes supporting long-term reversible stripping/deposition of magnesium metal in a low content or halide-free electrolyte are still of great interest. Moreover, the electrolytes should possess certain properties to be a good match with candidate cathode materials. Herein, the electrochemical performance of a novel indolyl-based electrolyte is presented. Theoretical modeling combined with NMR analysis identifies the magnesium species in the electrolyte. Reversible stripping/deposition of Mg metal in indolyl-based electrolyte shows long-term cycling with high coulombic efficiency of >99.5% and yields dendrite-free magnesium deposition in compact and smooth layers. The X-ray diffraction shows different preferential structural orientations depending on the electrode substrate. Finally, a proof-of-concept Mg||Mo₆S₈ full cell using the newly developed electrolyte is proposed.

1. Introduction

Lithium-ion batteries (LIBs) have an impact on our daily life since the turn of the nineties as the most important and widespread electrochemical energy storage systems.

S. Zaubitzer, S. Dongmo, M. Wohlfahrt-Mehrens, M. Marinaro
Zentrum für Sonnenenergie und Wasserstoff-Forschung
Baden-Württemberg
89081 Ulm, Germany
E-mail: mario.marinaro@zsw-bw.de

P. Schüler, S. Krieck, M. Westerhausen
Institute of Inorganic and Analytical Chemistry
Friedrich-Schiller University Jena
07743 Jena, Germany

F. Fiesinger, D. Gaissmaier, M. van den Borg, T. Jacob
Institute of Electrochemistry
Ulm University
89081 Ulm, Germany

D. Gaissmaier, T. Jacob, M. Wohlfahrt-Mehrens
Helmholtz Institute Ulm (HIU) Electrochemical Energy Storage
Helmholtz Str. 11, D-89081 Ulm, Germany

D. Gaissmaier, T. Jacob
Karlsruhe Institute of Technology (KIT)
76021 Karlsruhe, Germany

Nowadays, there is a continuously growing demand for higher energy density storage devices and for new sustainable battery technologies.^[1] Moreover, the development and implementation of new sustainable energy systems could become the ultimate bridge to a definitive energy transition, addressing increasingly pressing climate change problems. Magnesium (Mg) possesses the highest volumetric capacity (3850 mAh cm⁻³) compared to Li (2060 mAh cm⁻³), Na (1130 mAh cm⁻³), and Ca (2050 mAh cm⁻³), which makes a Mg metal-based battery cell a promising candidate to envision a future shift of the current battery field to a postlithium age.^[2,3] Moreover, depending on the experimental conditions, electrodeposition of metallic Mg can be free of dendrites.^[2,4-7] Abundancy, low cost, and eco-friendliness

are additional appealing features that render Mg metal an attractive choice.^[2,3,5-9] The first proof-of-concept of a rechargeable Mg metal battery was demonstrated by Aurbach et al., with the most impressive cycle life ever reported so far.^[10] Stripping and deposition of a magnesium metal anode were enabled for >3500 cycles using a Chevrel phase (CP) cathode.^[11] The organo-magnesium chloroaluminate complex, Mg(AlCl₂BuEt)₂/tetrahydrofuran (THF) was used as electrolyte, even if it presents now well-known corrosivity of the current collector and a limited anodic stability.^[12] The electrolyte contained Grignard reagents, making it nucleophilic in nature, and thus unsuitable for electrophilic-type cathode materials.^[13] This remarkable breakthrough of the first Mg battery prototype ignited a great interest in the development of suitable electrolytes and cathodes to improve the cell voltage. Intensive research has been carried out on the development of new electrolytes, which can enable reversible deposition and stripping at low overpotentials, are noncorrosive and nonnucleophilic in nature, possess high anodic stability, and are easy-to-make. However, the strategy to design compatible electrolytes that fulfill all these requirements seems not to be an easy task. A good compromise was found in the hexamethyldisilazide magnesium chloride (HMDSMgCl) electrolyte, as the addition of aluminum chloride (AlCl₃) improved the anodic stability up to 3.6 V versus Mg/Mg²⁺ on Pt.^[14] Worth noting that a high ratio of AlCl₃ Lewis acid and/or MgCl₂ in (HMDS)MgCl-based electrolytes leads not only to higher anodic stability but also to high Mg deposition

overpotential (up to 500 mV).^[15] Moreover, during reversible deposition of Mg metal using (HMDS)MgCl-based electrolyte formulation less than 100 cycles were reported, even in a full cell Mg||Mo₆S₈, considered as a state-of-art of Mg batteries.^[15] The introduction of the all-inorganic magnesium aluminum chloride (MACC) in THF or glyme electrolyte came shortly after as a breath of fresh air toward suitable Mg electrolytes. But still they are corrosive due to the high content of chloride ions^[15] and the electrodeposited Mg layer also contains aluminum and chlorine.^[16,17] Halide-free boron-centered carborane Mg(CB₁₁H₁₂)₂/tetraglyme (TG) and the tetrakis(hexafluoroisopropoxy)borate Mg[B(hfip)₄]₂/1,2-dimethoxyethane (DME) state-of-the-art electrolytes offer a high anodic stability \approx 3.90 V and 4.30 V versus Mg/Mg²⁺ on stainless steel (SS) and, due to the weakly coordinated anion, good ionic conductivities.^[18,19] Further improvements are, however, needed in terms of coulombic efficiency (\approx 94.4% and 98.0% for 0.4 M Mg(CB₁₁H₁₂)₂/TG and 0.6 M Mg[B(hfip)₄]₂/DME, respectively) cycling stability (up to 100 cycles reported for both types of electrolytes) and easier synthesis approaches.^[15,20–23] An additional challenge arises in the quest for a suitable cathode material.^[24] Intercalation of Mg²⁺ cations using metal oxide, sulfur, and selenide-based cathode materials presents many hurdles, owing to the high charge density of the Mg²⁺ divalent cation, leading to sluggish kinetics, which require high energies during desolvation processes at the electrode/electrolyte interface and during solid-state diffusion. Polyanionic structures are becoming more and more popular as cathode materials for Mg-batteries due to a strong inductive effect, which reduces the interaction with the guest Mg²⁺ cation.^[24–26] Conversion-type cathodes, such as sulfur (S), appear to be a possible alternative, owing to a comparable volumetric capacity when paired with a magnesium metal anode (3459 mAh cm³) and do not require a highly anodically stable electrolyte (up to \approx 2.5 V vs Mg/Mg²⁺).^[27,28] However, so far, the full proof-of-concept of a working Mg–sulfur battery using the state-of-art Mg[B(hfip)₄]₂/DME electrolyte showed 80% of capacity loss after 100 cycles,^[21] owing to the incompatibility with the electrolyte and a poor cyclability of the Mg anode.^[21,29] Therefore, an electrolyte allowing a prolonged stable cyclability of a Mg anode will be a step forward toward a practical Mg–S battery. To achieve this goal, we recently developed a nonnucleophilic HMDS-based electrolyte enabling a prolonged metal anode cycling, with a low halide content, and possessing relatively good anodic stability, required for Mg–S battery.^[30] The impact on the electrochemical performance by using halides strongly depends on the nature of the halide. So far, chloride has been the halide of choice for most formulations. However, it has been demonstrated that long-term cycling at high coulombic efficiencies can be achieved by using bromide instead of chloride,^[30] thus having a less corrosive environment.

In this work, we report a novel nonnucleophilic (indolyl) magnesium bromide electrolyte (Mg(Ind)Br). The in situ-Grignard metalation synthesis route yields one major Mg species. NMR spectroscopy characterization results are in line with theoretical simulations. Long-term reversible Mg deposition/stripping investigations show high coulombic efficiencies and low overpotentials without any addition of Lewis acids or

halide-based additives. Furthermore, in a full cell setup the electrolyte allows the intercalation and deintercalation of Mg²⁺ with a CP as cathode.

2. Results and Discussion

2.1. Magnesium Speciation Analysis and Modeling

Mg(Ind)Br was prepared using the in situ-Grignard metalation method (iGMM)^[31] starting from Mg metal, indole, and ethyl bromide. This highly efficient low costs (cf., Table S1, Supporting Information), one-pot reaction (yield up to >95%) provides an excellent synthetic route and allows preparing highly concentrated solutions. The solution structure was elucidated using standard NMR techniques (Figure S1–S5, Supporting Information) in combination with ECC-DOSY^[32] (Figure S6 and S7, Supporting Information) to determine the molar mass. In a Schlenk-type equilibrium, amido-magnesium halides typically coexist in solution with the corresponding homoleptic species [Equation (1)]. Surprisingly, only one set of NMR resonances was observed in THF solution hinting toward the formation of the heteroleptic complex [(D₈]THF)₄Mg(Ind)Br, as shown in Figure S5, Supporting Information, (M_w : calc.: 541, found: 541 g mol⁻¹, $\Delta = 0\%$). The ²⁵Mg NMR spectrum showed a broad singlet ($\delta = 4.7$ ppm, $\omega = 288$ Hz) and based on linewidth broadening an asymmetric coordination sphere of the quadrupolar metal ion can be assumed.

Density functional theory (DFT) calculations were performed to confirm the NMR data as well as to determine solution structure and solvation energies of the various species involved in the Mg(Ind)Br-based electrolyte equilibria. As described in the literature, Mg cations are mostly coordinated in a sixfold octahedral environment,^[33–35] although fourfold and fivefold coordination structures were also found depending on the bulkiness of ligated Lewis bases.^[36,37] In the case of the electrolyte studied in this work, the central Mg cation is arranged in an octahedral environment with the counterions located in *trans* positions due to electrostatic reasons (cf., Figure 1). We found the highest solvation energy (E_{solv}) for Mg(Ind)Br with -481 kJ mol⁻¹ followed by MgBr₂ and Mg(Ind)₂ with solvation energies of -473 and -472 kJ·mol⁻¹, respectively (cf., Table 1). The solvation energies of the considered species are almost identical with a maximum solvation energy difference (ΔE_{solv}) of 9 kJ mol⁻¹ between Mg(Ind)Br and Mg(Ind)₂. The narrow solvation energy range is consistent with the observed Mulliken atomic charges of the Mg atom, which are (with values between 0.97 and 1.11e, depending on the electrolyte species and degree of solvation) very similar; the atomic charges of the THF oxygen atoms are even closer between -0.57 and $-0.60e$ (Table S3–S5, Supporting Information). The average solvation energies per THF molecule (see Table 1) in the first solvation shell vary between -108 and -104 kJ·mol⁻¹, which is comparable with the calculated value of -98 kJ·mol⁻¹ from Wan et al. for their tetra-coordinated dichloromagnesium complex.^[36] As shown in Figure 1, a Schlenk-type equilibrium reaction takes place between two Mg(Ind)Br molecules on one side and one Mg(Ind)₂ + one MgBr₂ species on the other side [Equation (1)]

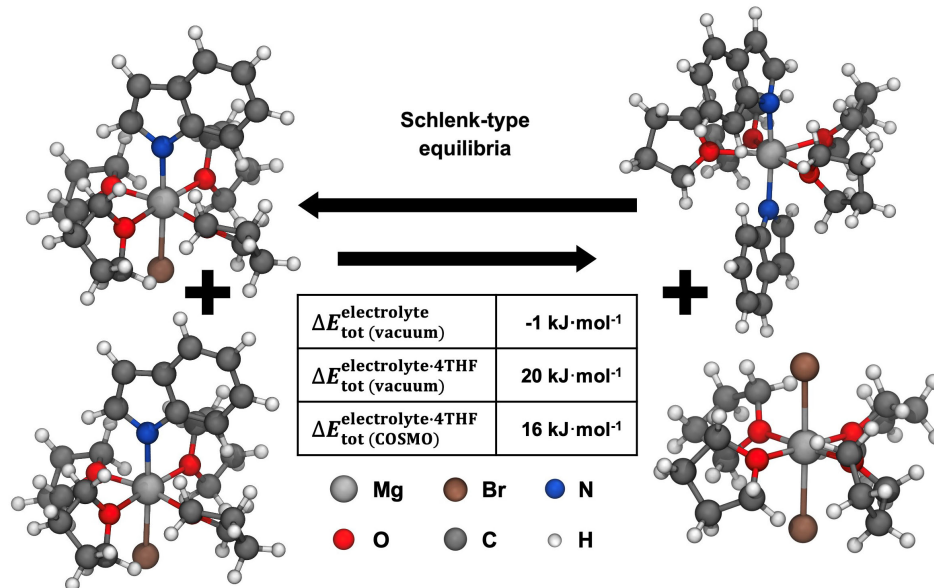


Figure 1. Schlenk-type equilibrium of the Mg(Ind)Br-based electrolyte. The first solvation shell consisting of four THF molecules was included explicitly, while additional THF solvation was considered implicitly using the conductor like screening model (COSMO).^[61] Two Mg(Ind)Br molecules are by $16 \text{ kJ}\cdot\text{mol}^{-1}$ ($20 \text{ kJ}\cdot\text{mol}^{-1}$ in case of only explicit THF solvation, $1 \text{ kJ}\cdot\text{mol}^{-1}$ in case of no solvation) thermodynamically more favorable compared to the educts $\text{Mg}(\text{Ind})_2 + \text{MgBr}_2$, indicating the position of the equilibrium shifted to the left side in line with the NMR analysis. The energy difference is defined as $\Delta E_{\text{tot}} = (E_{\text{tot}}^{\text{Mg}(\text{Ind})_2} + E_{\text{tot}}^{\text{MgBr}_2}) - 2 \cdot E_{\text{tot}}^{\text{Mg}(\text{Ind})\text{Br}}$.

Table 1. Calculated solvation energies (E_{solv}) for Mg(Ind)Br, MgBr_2 and $\text{Mg}(\text{Ind})_2$ in THF using Equation (2), (3), and (4). The first solvation layer is included explicitly; further THF solvation is described via the implicit solvation model COSMO.^[61] The solvation energy difference (ΔE_{solv}) is given for MgBr_2 , and $\text{Mg}(\text{Ind})_2$ with respect to Mg(Ind)Br which has the highest solvation energy with $-481 \text{ kJ}\cdot\text{mol}^{-1}$. The average solvation energy per THF molecule is calculated for the first solvation shell as $E_{\text{solv}} \text{ per THF} = E_{\text{explicit}}/4$.

$\text{kJ}\cdot\text{mol}^{-1}$	E_{solv}	ΔE_{solv}	$E_{\text{solv}} \text{ per THF}$
Mg(Ind)Br·4THF	-481		-108
MgBr ₂ ·4THF	-473	8	-104
Mg(Ind) ₂ ·4THF	-472	9	-108



To determine the equilibrium of this reaction, the total energies of both sides of the reaction have been evaluated. The two Mg(Ind)Br molecules are thermodynamically favored by $16 \text{ kJ}\cdot\text{mol}^{-1}$ ($20 \text{ kJ}\cdot\text{mol}^{-1}$ in case of Mg^{2+} ions only solvated by four explicit THF molecules) compared to the educts $\text{Mg}(\text{Ind})_2 + \text{MgBr}_2$. This finding attests that the equilibrium should slightly be shifted in favor of the heteroleptic complexes, which is in agreement with the obtained NMR results. However, the small energy difference also suggests a fast equilibrium between the heteroleptic and homoleptic species in THF solution. Without solvation, the equilibrium is almost balanced ($\Delta E_{\text{tot}}^{\text{electrolyte}}(\text{vacuum}) = -1 \text{ kJ}\cdot\text{mol}^{-1}$), which reveals the important role of the THF solvent in the equilibrium reaction.

2.2. Electrochemical Performance and Electrode-Dependency of Mg deposition

Deposition/stripping is one of the key steps for a successfully operating metal-based battery. To evaluate the electrochemical reversibility of the metal deposition and dissolution in the indolyl-based electrolyte, we first performed cyclic voltammetry (CV) measurements.

Figure 2A–D shows the typical features of electrochemical reversible deposition and dissolution of Mg metal. The feasibility of the magnesium deposition/dissolution was evaluated on different metal substrates, i.e., copper (Cu), nickel (Ni), SS, and platinum (Pt). Despite the similar shapes of the CVs, the onset for the Mg deposition indicated a substrate-dependent process. At cycle #10, the overpotential for Mg deposition was -185 mV (Cu), -190 mV (Pt), $\approx -220 \text{ mV}$ (Al), -225 mV (Ni), and $\approx -250 \text{ mV}$ for SS. The low overpotentials for the Mg electrodeposition (less than 200 mV on Cu and Pt) are comparable to the reported values of the Mg(HMDS)Br-based electrolyte obtained with the same sweep rate.^[28] Current density of $\approx 2 \text{ mA}\cdot\text{cm}^{-2}$ on Pt, SS, Ni and $-1.5 \text{ mA}\cdot\text{cm}^{-2}$ for Cu were reached at the cutoff potential of -0.8 V versus Mg/Mg^{2+} , respectively, at CV cycle #10. Cathodic current density values increased for Cu, Pt, SS and remained constant in the case of Ni electrode, at cycle #200. This casts a hint toward substrate-dependent processes that can slightly influence the electrochemical performance. Atomic force microscopy (AFM) (Figure 3) investigations of the Cu electrode roughness before and after cycling showed that this increase cannot be directly linked to an increased active surface of the working electrode because the changes in surface roughness (fresh: $R_z = 0.48 \pm 0.12 \mu\text{m}$,

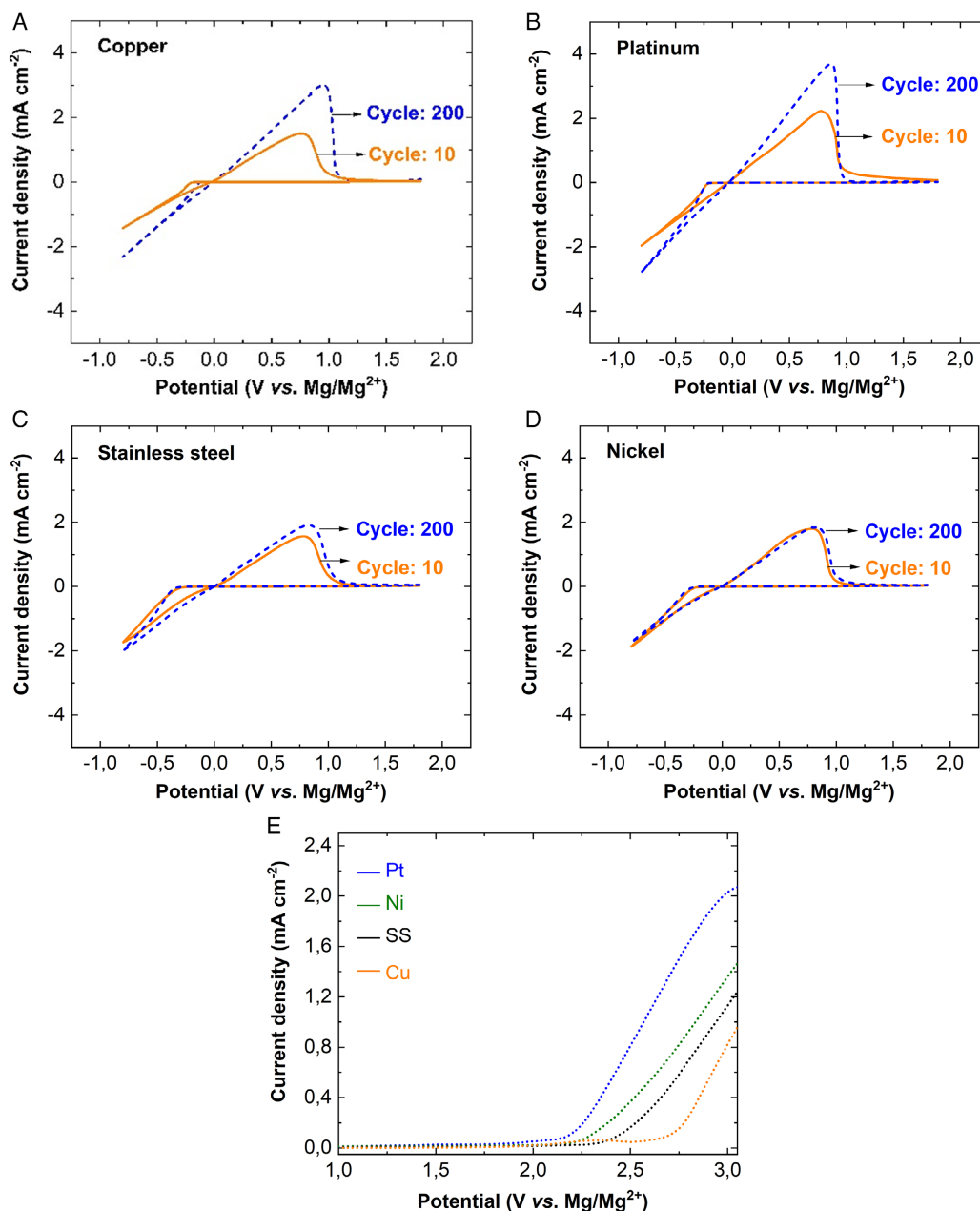


Figure 2. Cyclic voltammograms of the Mg electrodeposition and electrostripping process using 0.6 M Mg(Ind)Br in THF as electrolyte at various current collectors: A) Cu, B) Pt, C) SS, and D) Ni. Sweep rate of 10 mV s⁻¹. E) Linear sweep voltammograms at a sweep rate of 5 mV s⁻¹. All the electrochemical measurements were performed in a three-electrode setup with Mg as counter and reference electrodes.

cycled: $R_z = 0.52 \pm 0.9 \mu\text{m}$) are relatively small (cf., Figure S8 and S9, Supporting Information, for Pt, SS, and Ni, respectively). The anodic stability on different substrates was determined by linear sweep voltammetry (LSV). Figure 2E presents the anodic stabilities at a scan rate of 5 mV s⁻¹ and demonstrates comparatively good anodic stability on Cu (≈ 2.2 V vs Mg/Mg²⁺), Ni (2.3 V vs Mg/Mg²⁺), and SS (2.4 V vs Mg/Mg²⁺), similar to the reported values for nitrogen-based magnesium electrolytes containing strong Lewis-acid like aluminum chloride (AlCl₃)^[38] and moreover an improvement in the electrolyte stability of approximately

400 mV compared to the all-phenyl-complex and MACC electrolytes obtained on a SS current collector and same sweep rate.^[39] It is known that the anodic stability of nitrogen-based Mg electrolytes is governed by the N–Mg bond and can be improved through the stabilization of the bond by using a strong Lewis acid like AlCl₃.^[38] However, this could not be extended to the Mg(Ind)Br electrolyte, where an increase of current densities was observed due to the increase of the electrolyte conductivity from 0.46 mS cm⁻¹ (without AlCl₃) to 0.70 mS cm⁻¹ (with 10 mol% AlCl₃), as shown in Figure S10, Supporting Information. The

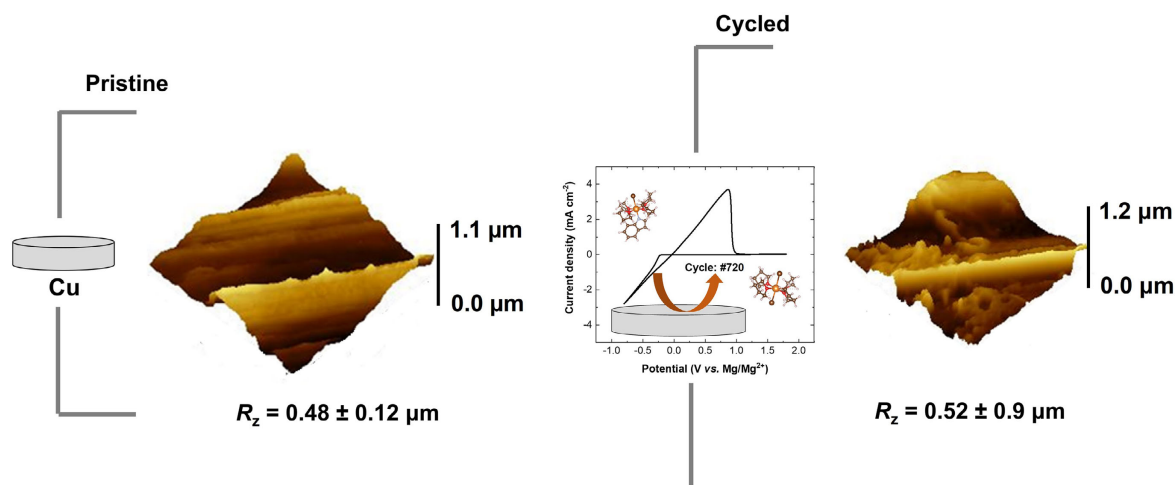


Figure 3. AFM characterization of the surface roughness of pristine and cycled Cu electrode.

addition of higher amounts of AlCl_3 yielded gel-type electrolytes and magnesium chloride (MgCl_2) or magnesium bromide (MgBr_2) does not dissolve in $\text{Mg}(\text{Ind})\text{Br}\text{-THF}$ electrolyte.

Long-term cycling at high coulombic efficiency can be a reliable indicator of stability and cyclability of electrolyte with the Mg metal anode and can be used to assess the electrochemical performance of novel electrolytes.^[30] For an accurate determination of the coulombic efficiency during the reversible Mg deposition/stripping process, chronopotentiometry technique was applied.^[40] **Figure 4A** shows the galvanostatic cycling of the indolyl-based electrolyte on Cu substrate at 0.8 mA cm^{-2} current density, with a timescale of 30 min during Mg deposition, and 0.8 V (vs Mg/Mg^{2+}) cutoff potential during stripping. The corresponding coulombic efficiencies up to cycle #700 are reported in **Figure 4B**. A remarkable coulombic efficiency of 99.5% is obtained during long-term cycling. This result is even more meaningful when compared with the available literature, which usually shows a cyclability of only 500 cycles, but nevertheless reported for a lower current density of about 0.5 mA cm^{-2} .^[41–43] This long-term stable cycling demonstrates

a remarkable stability of the electrolyte. A similar performance was observed with Pt, Ni, SS, and Al substrates (cf., **Figure S11** and **S12**, Supporting Information).

The electrodeposited Mg was characterized through scanning electron microscopy (SEM) and X-Ray diffraction (XRD). **Figure 5A–D** shows the XRD patterns of the deposited Mg metal layer on different substrates. The XRD pattern is characterized by sharp reflections which have been assigned to hexagonal Mg^[44] (PDF 00-035-0821) and to the metal substrates used as current collectors (Cu, SS, Ni, Pt). In the case of Ni and SS, the patterns of the substrate itself are missing because the deposited Mg layer could be easily removed from the metal substrate. SEM micrographs (**Figure 6A–E**) show different morphologies of electrodeposited Mg. In the case of a Cu electrode (**Figure 6A**), Mg deposits in regular shapes with different preferential orientations compared to Ni and SS. These observations are consistent if the intensity ratio of the $[002]/[101]$ XRD reflections of the electrodeposited Mg is taken into consideration. This aspect will be discussed in detail in the discussion section. The deposition onto Pt represents an exception, with Mg growth leading to a dense

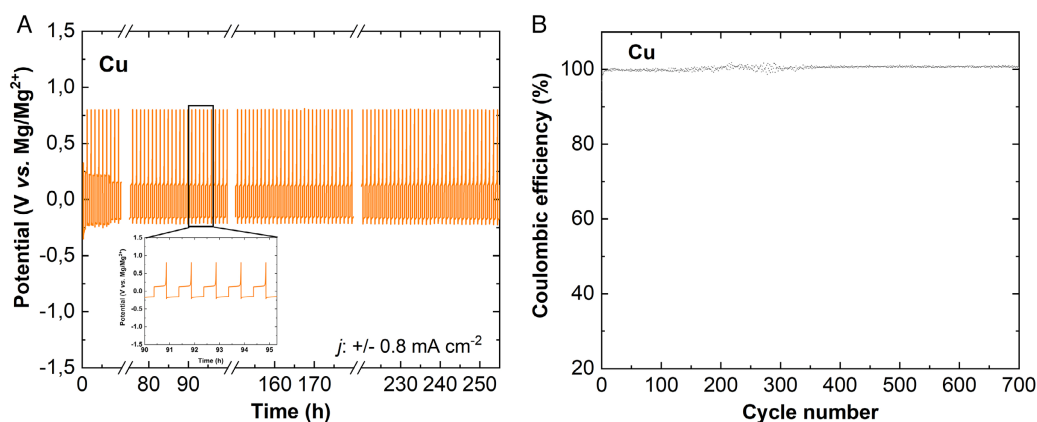


Figure 4. A) Chronopotentiometry cycling at Cu electrode using $0.6 \text{ M Mg}(\text{Ind})\text{Br}$ in THF at $\pm 0.8 \text{ mA cm}^{-2}$ with 30 min time scale during deposition and cutoff potential at 0.8 V during stripping, Mg was used as reference and counter electrode. B) Coulombic efficiencies evaluated after chronopotentiometry measurement.

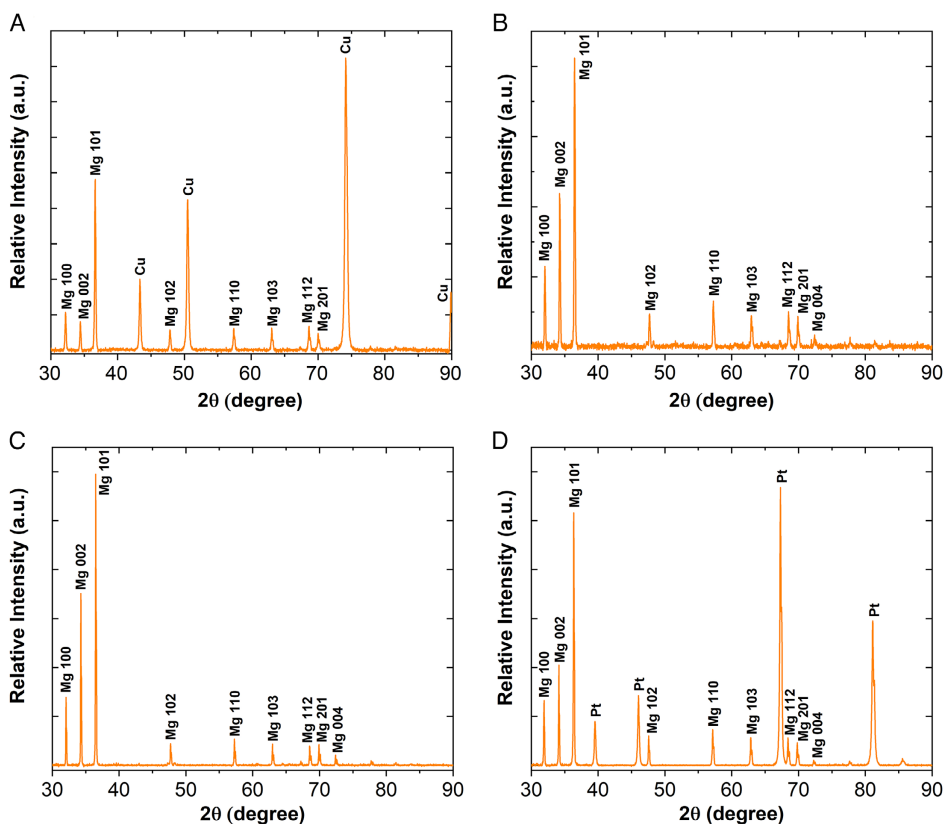


Figure 5. XRD patterns of deposited magnesium layer on A) Cu, B) SS, C) Ni, and D) Pt obtained after chronoamperometry at 350 mV with 3.93 mAh cm^{-2} as limited capacity.

and homogenous layer. SEM images of the Pt-deposited Mg layer are devoid of the current collector because it was found to be easily removable from the substrate after XRD analysis (Figure 6D). From the respective cross-sectional view (Figure 6E), also residual glass fibers on top of the thick Mg layer can be identified.

As a proof-of-concept, a full cell Mg battery with Mo_6S_8 as a cathode and Mg foil as anode was assembled. The resulting charge-discharge profiles of the Mo_6S_8 cathode, using 2 mA g^{-1} as current density, are presented in Figure 7A. At cycle #2, a discharge capacity of 40 mAh g^{-1} is achieved and further increases to around 50 mAh g^{-1} at cycle #14 (cf., Figure 7A,C) with a high overall reversibility for the de-/intercalation process (cf., Figure 7D, for the cycling performance, cf., Figure S13A,B, Supporting Information). Such a rise in the capacity during cycling can be assigned to improving the Mg diffusivity in the host material caused by the increasing amount of inserted Mg^{2+} ions in the lattice of the CP.^[45] Furthermore, the Mg can also be plated and stripped at the anode side at low overpotentials (cf., Figure 7B).

Also is the solvation environment for the Mg^{2+} ions strongly connected to the de- and intercalation into the CP. The cycling profile shows a slow diffusion kinetics as also reported by Ren *et al.*^[42] Nevertheless, besides the similarly shape of the charge-discharge curves for the de-/intercalation of magnesium ions into the host material, the different states of charge are investigated by XRD (cf., Figure S14, Supporting Information)

and in good agreement with the data reported in the literature.^[46,47]

3. Discussion

Lewis acid salt AlCl_3 added in $\text{Mg}(\text{Ind})\text{Br}\cdot\text{THF}$ does not improve the anodic stability of this novel electrolyte formulation (cf., Figure S1C, Supporting Information) as reported for HMDS-based electrolytes.^[48] Therefore, an extension to other nitrogen-containing electrolytes cannot be considered in this case. Moreover, the nonnucleophilicity of the benzopyrrole anion is influenced by the solvent. Depending on the solvent, aprotic polar or nonpolar, the benzopyrrole anion can produce a nucleophilic attack or not.^[45] This could stand as a starting point to optimize the $\text{Mg}(\text{Ind})\text{Br}$ by testing the impact of different compatible solvents on the electrochemical performance of the electrolyte at different concentrations. Deposition and stripping processes have been shown to be substrate-dependent processes, affecting the overpotential and current densities of Mg electrodeposition and the preferential orientation of the crystalline structure. A tentative explanation of the substrate dependence can be done considering their intrinsic properties, such as the electronic conductivity and the affinity between Mg and the substrate during the nucleation processes at the atomic scale (surface energy). The impact of the electrolyte interface generated during the deposition process or the generation of new electrochemically active

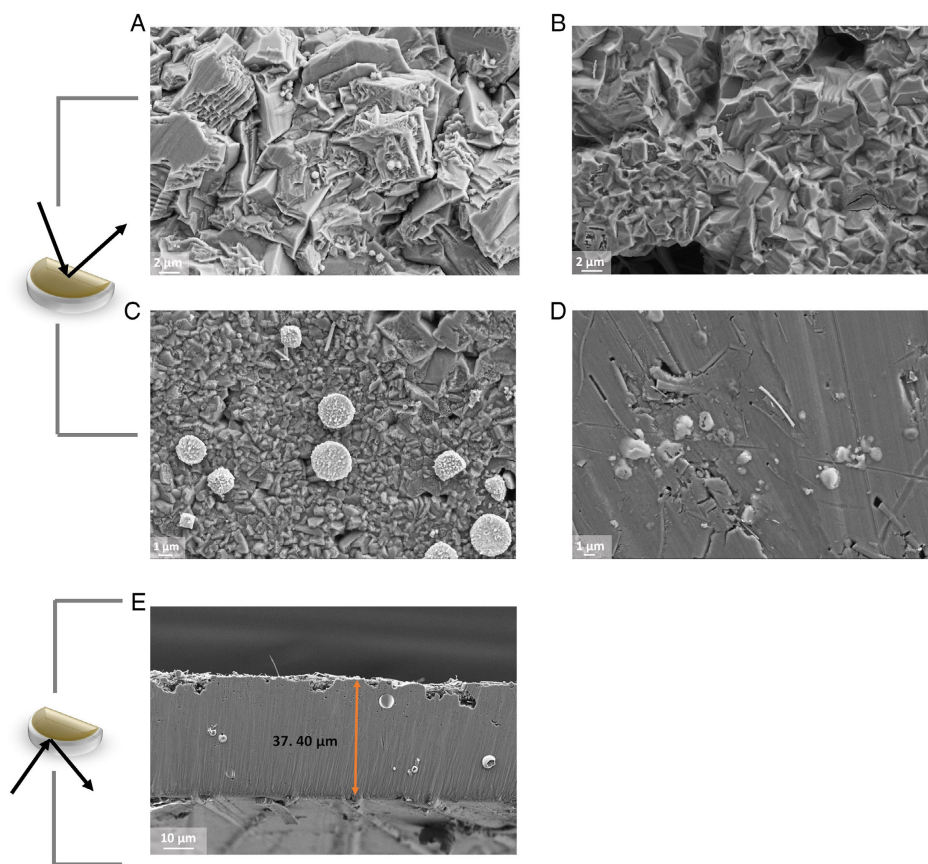


Figure 6. Scanning electron micrographs of deposited magnesium layer on A) Cu electrode, B) (SS), C) Ni, D) Pt, and E) cross-sectional view of pure Mg layer deposited on Pt.

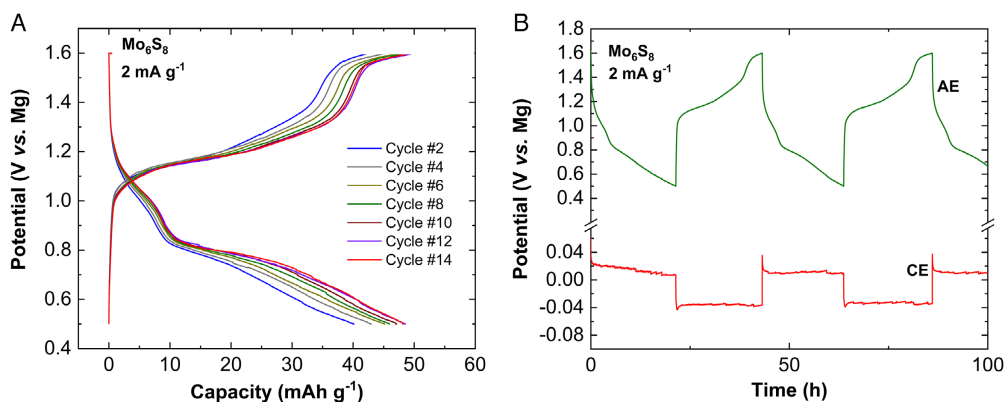


Figure 7. Galvanostatic cycling of the $\text{Mg}||0.6 \text{ M Mg(Ind)Br/THF}||\text{Mo}_6\text{S}_8$ cell cycled at 2 mA g^{-1} in a three-electrode setup with an Mg quasireference electrode and a cutoff voltage of 0.5–1.6 V. A) Charge/discharge profiles of the Mo_6S_8 working electrode and the B) enlarged graph of the voltage profiles of the Mo_6S_8 working electrode (green) and Mg counter electrode (red).

Mg-species during cycling could eventually explain the increase of current density. The different orientations of a crystalline structure during electrodeposition of Mg on Ni, SS, and Pt operate by minimizing the surface energy, reflected in the high-intensity [002] plane compared to [100]. Cu shows a lower intensity for the respective orientation, and as mentioned above, the surface energy cannot be minimized during crystal growth

thus the preferential orientation is along the [100] plane.^[49] It has been reported that the high-intensity ratio [002]/[101] indicates that the crystal growth proceeds preferentially along the ab plane and vice versa; a low-intensity ratio indicates a growth along the c-axis.^[49] The peak ratio increases from Cu (0.17), Ni (1.69), SS (1.90) to Pt (2.5), and it is consistent with the observed morphological differences in the deposited Mg layers. The

energetically different surface orientations during the crystal growth are presented in the different reflection intensities for the electrodeposited Mg.^[50] Furthermore, low intensity for the [002] reflection indicates a low tendency to minimize surface energy^[49] during the crystal growth on Cu. Although [101] shows the highest reflection intensity in the XRD pattern, it possesses the highest surface energy compared to the [100] and [002] orientation. These can be explained by the highest area fraction from the [101] orientation in the crystal's equilibrium shape and underpins the theoretical findings of Lautar et al.^[50] Mechanistically speaking, the electrodeposition of Mg seems not to be a simple two-electron transfer.^[51] It is rather a complicated adsorption process that is influenced by the electrochemically active species.^[52] In the case of organomagnesium chloroaluminate electrolytes, the electrochemical-active species in solution comprises a dimeric magnesium-cationic complex $[\text{Mg}_2(\mu\text{-Cl}_3)*6\text{THF}]^+$.^[53] Analytical approaches such as in situ/operando-X-Ray absorption spectroscopy (XAS) demonstrated that on the electrode surface, the dimeric complex splits into a mononuclear cationic complex $[\text{MgCl}*5\text{THF}]^+$.^[54] In the case of HMDS-based electrolytes, several active species are present in solution and are subject to a Schlenk-type equilibrium.^[27,30] Due to the presence of such equilibria, theoretical forecasts (e.g., DFT-based simulations) become much more complicated. Nevertheless, future works should be conducted to validate the electrochemically active species during the polarization of the electrode, e.g., by in situ-Raman or electrochemical NMR. Furthermore, more details about the nucleation and preferential growth directions are needed and should be investigated, e.g., with electrochemical scanning tunnel microscopy (STM).

4. Conclusions

In summary, we report on the electrochemical performance of a novel electrolyte for Mg-ion batteries containing benzopyrrole and bromide as anions. The high performance through deposition and stripping does not require additional Lewis acids such as AlCl_3 or halide-based additives. As suggested by XRD characterization, the deposited magnesium layers present different preferential growth orientations, depending on the substrates. The analysis of Mg species reveals the formation of a Schlenk-type equilibrium. It identifies $(\text{thf})_4 \text{Mg}(\text{Ind})\text{Br}$ as the main bulk species, which is in line with the theoretical calculation of solvation-desolvation energies. Furthermore, this benzopyrrole-based electrolyte allows the de- and intercalation of Mg^{2+} into a CP cathode. Moreover, after long-term cycling, there is no indication of corrosion at the current collector. This electrolyte is very promising for application in the next generation of rechargeable Mg batteries with good electrochemical performance and the one-pot cost-effective synthesis.

5. Experimental Section

Computational Details: The input structures for the electrolytes were generated with the AMS driver program^[55] and preoptimized with a modified version of the semiempirical PM7 method^[56] as implemented in the MOPAC engine.^[57] All first principles geometry optimizations were performed within the Amsterdam Density Functional (ADF)^[55] program

suite. Spin unrestricted, nonrelativistic calculations were performed using Slater-type orbitals (STOs) with triple zeta polarized (TZP), all-electron basis sets^[58] and the meta hybrid exchange-correlation functional MN15^[59] as part of the LibXC library.^[60] Self-consistent field (SCF) convergence was achieved when the energy difference between consecutive SCF cycles was less than $2.6 \times 10^{-3} \text{ kJ mol}^{-1}$, and the geometry was considered as converged when all forces were at least smaller than $2.6 \text{ kJ mol}^{-1} \cdot \text{\AA}^{-1}$. The THF solvation energy was calculated in a two-step process, with the first solvation shell included explicitly, while additional THF solvation was considered implicitly using the conductor like screening model (COSMO) as implemented in ADF^[61] [Equation (2)].

$$E_{\text{solv}} = E_{\text{explicit}} + E_{\text{implicit}} \quad (2)$$

The explicit fraction of THF solvation was calculated by subtracting the total energies of the respective electrolyte species ($\text{Mg}(\text{Ind})\text{Br}$, $\text{Mg}(\text{Ind})_2$, MgBr_2) and the THF molecules from the total energy of the electrolyte with the first solvation shell included [Equation (3)].

$$E_{\text{explicit}} = E_{\text{tot}(\text{vacuum})}^{\text{electrolyte-4THF}} - E_{\text{tot}(\text{vacuum})}^{\text{electrolyte}} - 4 \cdot E_{\text{tot}(\text{vacuum})}^{\text{THF}} \quad (3)$$

The implicit fraction of THF solvation corresponds to the difference in total energy from a COSMO and a vacuum calculation of the electrolyte with the first solvation shell included explicitly [Equation (4)].

$$E_{\text{implicit}} = E_{\text{tot}(\text{COSMO})}^{\text{electrolyte-4THF}} - E_{\text{tot}(\text{vacuum})}^{\text{electrolyte-4THF}} \quad (4)$$

Detailed absolute energies for the electrolyte species $\text{Mg}(\text{Ind})\text{Br}$, MgBr_2 , and $\text{Mg}(\text{Ind})_2$ involved in the calculation of the solvation energy E_{solv} may be found in Table S2, Supporting Information. Atomic charges were determined with the Mulliken charge analysis.^[62]

Electrolyte Synthesis and NMR/Mass Spectrometry Characterization: All manipulations were carried out in an inert nitrogen atmosphere using standard Schlenk techniques, if not otherwise noted. The solvents were dried over KOH and subsequently distilled over sodium/benzophenone in a nitrogen atmosphere before use. Deuterated THF was dried over sodium, distilled, degassed, and stored under nitrogen over sodium. All substrates were purchased from Alfa or TCI and used without further purification. The yields given are not optimized. NMR spectra were recorded using a Bruker Avance III 400 MHz and a Bruker Avance III 600 MHz spectrometer. Chemical shifts are reported in parts per million relative to SiMe_4 as an external standard referenced to the solvents residual proton signal. Molecular mass analysis via NMR spectroscopy was done using the Stalke method (ECC-DOSY,^[32] $[\text{D}_8]\text{THF}$ as internal standard) and the *ledbgp2s* pulse program. ASAP-HSQC-NMR spectra were recorded using the pulse program published by Luy.^[63]

Synthesis of IndMgBr : Magnesium (98%, granular, 0.41 g, 17.1 mmol) and indole (2.00 g, 1 eq., 17.1 mmol) were placed in a Schlenk flask and THF (25 mL) was added. EtBr (1.27 mL, 1 eq., 17.1 mmol) was added in three portions over 1 h. The reaction mixture was stirred for 3 h at room temperature. The solution was decanted from the unreacted magnesium and used without further purification (0.56 M, 83%, 14.1 mmol). The yield was determined by acidimetric titration of a hydrolyzed aliquot. ^1H NMR (400 MHz, $[\text{D}_8]\text{THF}$, 298 K) $\delta = 6.31$ (s, 1H, H3), 6.69 (t, $J = 7.19$ Hz, 1H, H5), 6.76 (dt, $J = 6.76, 0.97$ Hz, 1H, H6), 7.3 (s, br, H2), 7.40 (d, $J = 7.5$ Hz, H7), 7.50 (d, $J = 7.8$ Hz, H4) ppm. $^{13}\text{C}\{^1\text{H}\}$ NMR (101 MHz, $[\text{D}_8]\text{THF}$, 298 K) $\delta = 100.5$ (C3), 115.6 (C4), 116.6 (C5), 119.6 (C7), 132.0 (C3a), 135.3 (br, C2), 146.4 (C7a) ppm. ^{25}Mg -NMR (24.5 MHz, $[\text{D}_8]\text{THF}$, 297 K) $\delta = 4.7$ ppm (bs, $\omega = 288$ Hz), $^{15}\text{N}\{^1\text{H}\}$ NMR (MHz, $[\text{D}_8]\text{THF}$, 297 K) $\delta = 181.3$ (s).

Materials and Electrochemical Characterization: Copper foil (99.95%, $d = 0.01$ mm, Schlenk), magnesium foil (99.95%, $d = 0.15$ mm, Goodfellow), and magnesium wire (99.99%, $d = 1$ mm, Goodfellow) were used as working, counter, and reference electrodes, respectively. Furthermore, SS foil ($d = 0.025$ mm, Goodfellow), aluminum foil (Schlenk), nickel foil (99%, $d = 0.1$ mm, Goodfellow), and platinum foil (99.99%, $d = 0.1$ mm, Goodfellow) were used as working electrodes. Prior to use, the copper and aluminum foils were dried under vacuum

at 120 °C. To remove the thin native oxide layer onto the magnesium current collector, the surface was polished with sandpaper (1200 µm).

The Chevrel cathodes were prepared by homogenization of the powder mixture consisting of 70 wt% Mo₆S₈ (NEI Corporation USA), 20 wt% Super C65, and 10 wt% polyvinylidene fluoride (PVDF, Solvay) in a speed-mixer (DAC 800.2 VAC-P) for 1000 rpm (1 min), 1500 rpm (2 min), and 2000 rpm (2 min). Afterward 20 mL of *N*-methyl-2-pyrrolidone (NMP) was added to the powder and homogenized again each for 1 min at 1000, 1500, and 2000 rpm. The obtained slurry were coated on a copper foil and predried for 2 h at 80 °C. After being cut into $d = 18$ mm discs, the cathode was dried under vacuum at 80 °C for 15 h. The mass loading of CP was around 1.0–1.5 mg cm⁻².

The electrochemical measurements were performed inside a glove box using EL-Cell ECC-Ref cells. Cell assembling was done according to the following sequence: working and counter electrodes $d = 18$ mm, a piece of magnesium wire was used as reference electrode. A glass fiber used as separator (1.55 mm thick, ECC-01-0021-C/L, EL-Cell) used as reservoir for Mg electrolyte (450 µL). The electrochemical tests were performed on a BioLogic VMP3 cell test system with BioLogic EC-Lab software V10.32. CV experiments were run in a potential range between 0.8 V and 1.8 V versus Mg/Mg²⁺ at a scan rate of 10 mV s⁻¹. Linear sweep voltammetry (LSV) experiments were performed with copper, nickel, aluminum, SS, and platinum current collectors with a scan rate of 5 mV s⁻¹. Mg was electrodeposited onto the current collectors by using chronoamperometry at a fixed voltage of 350 mV to obtain 3.93 mAh cm⁻². Coulombic efficiencies have been calculated from chronopotentiometry experiments carried out at ±0.8 mA cm⁻² for $t = 30$ min and an upper cut-off of 0.8 V. Ionic conductivities were measured using a Microcell from HC-rhd instruments. It consists of a 4-platinum electrode setup and determines the conductivity by electrochemical impedance spectroscopy (EIS).

AFM Measurements: The topography of an uncycled Cu sample and one after 720 cycles was measured by an AFM (Topometrix Explorer with Anfatec Controller) using a Multi75GD-G cantilever (Budgetsensors, Sofia, Bulgaria). A 50 × 50 µm² area of the surface was then measured with a scan rate of 2 Hz.

XRD and SEM-EDX Characterization: XRD and SEM were applied to characterize the morphology of the electrodeposited Mg on the current collector. XRD pattern was recorded using an air-dome sample holder in a single scan between 10° and 90° in 0.02° 2θ increments on a Bruker AXS D8 Discover using Cu Kα radiation, a Ni-monochromator, and a LYNXEYE 2D energy dispersive detector. The SEM images have been obtained with a LEO 1530 VP microscope with an acceleration of 5.0 kV and a secondary electron detector.

Supporting Information

Supporting Information is available from the Wiley Online Library or from the author.

Acknowledgements

This work contributes to the research performed at CELEST (Center for Electrochemical Energy Storage Ulm-Karlsruhe) and was partly funded by the German Research Foundation (DFG) under Project ID 390874152 (POLIS Cluster of Excellence). The authors acknowledge support by the state of Baden-Württemberg through bwHPC and the German Research Foundation (DFG) through grant no. INST 40/575-1 FUGG (JUSTUS 2 cluster). S.Z., S.D., M.W.-M., and M.M. would also like to acknowledge the German Federal Ministry of Education and Research (BMBF) for financial support within the project “LuCaMag” (grant no. 03EK3051D). Additionally, T.J. gratefully acknowledges support by the German Science Foundation through the priority program SPP-2248. P.S. is very grateful to the German Environment Foundation (Deutsche Bundesstiftung Umwelt, DBU, grant no. 20018/578) for a generous Ph.D. grant. The authors acknowledge the valuable support of the NMR and the MS-platform of the Faculty of Chemistry and Earth

Sciences of the Friedrich Schiller University Jena, Germany. The authors thank also Dr. Maximilian Eckl for the AFM measurements, Dr. Claudia Pfeiffer for SEM measurements, Dagmar Wehrather-Köstner for ionic conductivity measurements, and Cornelius Gauckler who helped with the preparation of the Chevrel cathode. Finally, the authors thank to Dr. Fabio Maroni who critically read the manuscript and added helpful comments.

Conflict of Interest

The authors declare no conflict of interest.

Author Contributions

S.Z. and S.D. conducted the electrochemical measurements, XRD characterizations, and analyzed together with M.M. P.S. synthesized the electrolyte, collected all of the NMR data, and analyzed together with S.K. and M.W. F.F. performed all the calculations and analyzed together with D.G., M.B., and T.J. M.M., M.W., T.J., and M.W.M. supervised the research. The manuscript was written through contributions of all authors. All authors discussed the results and commented on the manuscript.

Data Availability Statement

The data that support the findings of this study are available from the corresponding author upon reasonable request.

Keywords

aprotic electrolytes, density functional theory, electrochemical metal deposition/dissolution, Mg-batteries, Schlenk-type equilibrium

- [1] M. Marinaro, D. Bresser, E. Beyer, P. Faguy, K. Hosoi, H. Li, J. Sakovica, K. Amine, M. Wohlfahrt-Mehrens, S. Passerini, *J. Power Sources* **2020**, 459, 228073.
- [2] J. Niu, Z. Zhang, D. Aurbach, *Adv. Energy Mater.* **2020**, 10, 2000697.
- [3] S. Passerini, D. Bresser, A. Moretti, A. Varzi, in *Batteries Present and Future Energy Storage Challenges*, Wiley-VCH, Weinheim **2020**.
- [4] N. Sa, B. Pan, A. Saha-Shah, A. A. Hubaud, J. T. Vaughey, L. A. Baker, C. Liao, A. K. Burrell, *ACS Appl. Mater. Interfaces* **2016**, 8, 16002.
- [5] K. Xu, *Chem. Rev.* **2004**, 104, 4303.
- [6] O. Crowther, A. C. West, *J. Electrochem. Soc.* **2008**, 155, A806.
- [7] R. Schwarz, M. Pejic, P. Fischer, M. Marinaro, L. Jörissen, M. Wachtler, *Angew. Chem. Int. Ed.* **2016**, 55, 14958.
- [8] N. N. Greenwood, A. Earnshaw, in *Chemie Der Elemente*, VCH-Verlagsgesellschaft MbH, Weinheim **1988**.
- [9] N. Sa, N. N. Rajput, H. Wang, B. Key, M. Ferrandon, V. Srinivasan, K. A. Persson, A. K. Burrell, J. T. Vaughey, *RSC Adv.* **2016**, 6, 113663.
- [10] D. Aurbach, Z. Lu, A. Schechter, Y. Gofer, H. Gizbar, R. Turgeman, Y. Cohen, M. Moshkovich, E. Levi, *Nature* **2000**, 407, 724.
- [11] D. Aurbach, I. Weissman, Y. Gofer, E. Levi, *Chem. Rec.* **2003**, 3, 61.
- [12] Y. Yang, W. Wang, Y. NuLi, J. Yang, J. Wang, *ACS Appl. Mater. Interfaces* **2019**, 11, 9062.
- [13] R. Deivanayagam, B. J. Ingram, R. Shahbazian-Yassar, *Energy Storage Mater.* **2019**, 21, 136.

- [14] Z. Zhao-Karger, X. Zhao, O. Fuhr, M. Fichtner, *RSC Adv.* **2013**, *3*, 16330.
- [15] Z. Zhang, S. Dong, Z. Cui, A. Du, G. Li, G. Cui, *Small Methods* **2018**, *2*, 1800020.
- [16] R. E. Doe, R. Han, J. Hwang, A. J. Gmitter, I. Shterenberg, H. D. Yoo, N. Pour, D. Aurbach, *Chem. Commun.* **2014**, *50*, 243.
- [17] G. Vardar, J. G. Smith, T. Thompson, K. Inagaki, J. Naruse, H. Hiramatsu, A. E. S. Sleightholme, J. Sakamoto, D. J. Siegel, C. W. Monroe, *Chem. Mater.* **2016**, *28*, 7629.
- [18] O. Tutusaus, R. Mohtadi, T. S. Arthur, F. Mizuno, E. G. Nelson, Y. V. Sevryugina, *Angew. Chem. Int. Ed.* **2015**, *54*, 7900.
- [19] Z. Zhao-Karger, M. E. Gil Bardaji, O. Fuhr, M. Fichtner, *J. Mater. Chem. A* **2017**, *5*, 10815.
- [20] H. Shuai, J. Xu, K. Huang, *Coord. Chem. Rev.* **2020**, *422*, 213478.
- [21] Z. Zhao-Karger, R. Liu, W. Dai, Z. Li, T. Diemant, B. P. Vinayan, C. Bonatto Minella, X. Yu, A. Manthiram, R. J. Behm, M. Ruben, M. Fichtner, *ACS Energy Lett.* **2018**, *3*, 2005.
- [22] J. Luo, Y. Bi, L. Zhang, X. Zhang, T. L. Liu, *Angew. Chem. Int. Ed.* **2019**, *58*, 6967.
- [23] T. Mandai, *ACS Appl. Mater. Interfaces* **2020**, *12*, 39135.
- [24] F. Maroni, S. Dongmo, C. Gauckler, M. Marinaro, M. Wohlfahrt-Mehrens, *Batter. Supercaps* **2021**, *4*, 1221.
- [25] G. Hasegawa, Y. Akiyama, M. Tanaka, R. Ishikawa, H. Akamatsu, Y. Ikuhara, K. Hayashi, *ACS Appl. Energy Mater.* **2020**, *3*, 6824.
- [26] S. Dongmo, F. Maroni, C. Gauckler, M. Marinaro, M. Wohlfahrt-Mehrens, *J. Electrochem. Soc.* **2021**, *168*, 120541.
- [27] H. S. Kim, T. S. Arthur, G. D. Allred, J. Zajicek, J. G. Newman, A. E. Rodnyansky, A. G. Oliver, W. C. Boggess, J. Muldoon, *Nat. Commun.* **2011**, *2*, 426.
- [28] Z. Zhao-Karger, R. Liu, W. Dai, Z. Li, T. Diemant, B. P. Vinayan, C. Bonatto Minella, X. Yu, A. Manthiram, R. J. Behm, M. Ruben, M. Fichtner, *ACS Energy Lett.* **2018**, *3*, 2005.
- [29] D.-T. Nguyen, R. Horia, A. Y. S. Eng, S.-W. Song, Z. W. Seh, *Mater. Horizons* **2021**, *8*, 830.
- [30] S. Dongmo, S. Zaubitzer, P. Schüler, S. KriECK, L. Jörissen, M. Wohlfahrt-Mehrens, M. Westerhausen, M. Marinaro, *ChemSusChem* **2020**, *13*, 3530.
- [31] S. KriECK, P. Schüler, J. Peschel, M. Westerhausen, *Synthesis* **2019**, *51*, 1115.
- [32] R. Neufeld, D. Stalke, *Chem. Sci.* **2015**, *6*, 3354.
- [33] M. Pavlov, P. E. M. Siegbahn, M. Sandström, *J. Phys. Chem. A* **1998**, *102*, 219.
- [34] K. Fujii, M. Sogawa, N. Yoshimoto, M. Morita, *J. Phys. Chem. B* **2018**, *122*, 8712.
- [35] T. Kimura, K. Fujii, Y. Sato, M. Morita, N. Yoshimoto, *J. Phys. Chem. C* **2015**, *119*, 18911.
- [36] L. F. Wan, D. Prendergast, *J. Am. Chem. Soc.* **2014**, *136*, 14456.
- [37] P. Schüler, S. Sengupta, S. Zaubitzer, F. Fiesinger, S. Dongmo, H. Görls, M. Wohlfahrt-Mehrens, M. Borg, D. Gaissmaier, S. KriECK, M. Marinaro, T. Jacob, M. Westerhausen, *Eur. J. Inorg. Chem.* **2022**, 2022.
- [38] X. Zhao, Y. Yang, Y. Nuli, D. Li, Y. Wang, X. Xiang, *Chem. Commun.* **2019**, *55*, 6086.
- [39] A. L. Lipson, S.-D. Han, B. Pan, K. A. See, A. A. Gewirth, C. Liao, J. T. Vaughey, B. J. Ingram, *J. Electrochem. Soc.* **2016**, *163*, A2253.
- [40] Y. Liang, H. Dong, D. Aurbach, Y. Yao, *Nat. Energy* **2020**, *5*, 646.
- [41] J. T. Herb, C. A. Nist-Lund, C. B. Arnold, *ACS Energy Lett.* **2016**, *1*, 1227.
- [42] W. Ren, D. Wu, Y. NuLi, D. Zhang, Y. Yang, Y. Wang, J. Yang, J. Wang, *ACS Energy Lett.* **2021**, *6*, 3212.
- [43] X. Huang, J. Wen, J. Lei, G. Huang, F. Pan, L. Li, *ACS Appl. Mater. Interfaces* **2022**, *14*, 8906.
- [44] H. E. Swanson, E. Tatge, Nat. Bur. Stand. Rep. (ICDD PDF No. 00-004-0770), **1953**.
- [45] E. Levi, G. Gershinsky, D. Aurbach, O. Isnard, G. Ceder, *Chem. Mater.* **2009**, *21*, 1390.
- [46] M. D. Levi, D. Aurbach, *J. Power Sources* **2005**, *146*, 349.
- [47] E. Levi, A. Mitelman, O. Isnard, M. Brunelli, D. Aurbach, *Inorg. Chem.* **2008**, *47*, 1975.
- [48] R. Attias, M. Salama, B. Hirsch, Y. Goffer, D. Aurbach, *Joule* **2019**, *3*, 27.
- [49] M. Matsui, *J. Power Sources* **2011**, *196*, 7048.
- [50] A. Kopač Lautar, D. Kopač, T. Rejec, T. Bančič, R. Dominko, *Phys. Chem. Chem. Phys.* **2019**, *21*, 2434.
- [51] K. Ta, K. A. See, A. A. Gewirth, *J. Phys. Chem. C* **2018**, *122*, 13790.
- [52] D. Aurbach, A. Schechter, M. Moshkovich, Y. Cohen, *J. Electrochem. Soc.* **2001**, *148*, 1004.
- [53] D. Aurbach, H. Gizbar, A. Schechter, O. Chusid, H. E. Gottlieb, Y. Gofer, I. Goldberg, *J. Electrochem. Soc.* **2002**, *149*, 115.
- [54] A. Benmayza, M. Ramanathan, T. S. Arthur, M. Matsui, F. Mizuno, J. Guo, P. A. Glans, J. Prakash, *J. Phys. Chem. C* **2013**, *117*, 26881.
- [55] R. Rüger, M. Franchini, T. Trnka, A. Yakovlev, E. van Lenthe, P. Philippen, T. van Vuren, B. Klumpers, T. Soini, *AMS 2020.101, SCM, Theoretical Chemistry*, Vrije Universiteit, Amsterdam, The Netherlands, <https://www.scm.com> (accessed: June 2022).
- [56] J. J. P. Stewart, *J. Mol. Model.* **2013**, *19*, 1.
- [57] J. J. P. Stewart, AMS MOPAC 2020, MOPAC Engine based on the MOPAC2016 source code, <http://OpenMOPAC.net> (accessed: June 2022).
- [58] D. P. Chong, E. Van Lenthe, S. Van Gisbergen, E. J. Baerends, *J. Comput. Chem.* **2004**, *25*, 1030.
- [59] H. S. Yu, X. He, S. L. Li, D. G. Truhlar, *Chem. Sci.* **2016**, *7*, 5032.
- [60] S. Lehtola, C. Steigemann, M. J. T. Oliveira, M. A. L. Marques, *SoftwareX* **2018**, *7*, 1.
- [61] C. C. Pye, T. Ziegler, *Theor. Chem. Acc. Theory, Comput. Model.* **1999**, *101*, 396.
- [62] R. S. Mulliken, *J. Chem. Phys.* **1955**, *23*, 1833.
- [63] D. Schulze-Sünninghausen, J. Becker, B. Luy, *J. Am. Chem. Soc.* **2014**, *136*, 1242.